Sensors & Actuators: B. Chemical 386 (2023) 133726

Contents lists available at ScienceDirect

Sensors and Actuators: B. Chemical

journal homepage: www.elsevier.com/locate/snb

Conductometric sensor for gaseous sulfur-mustard simulant by gold nanoparticles anchored on ZnO nanosheets prepared via microwave irradiation

Minkyung Lee [a,b,1], Min Young Kim [a,1], Jihee Kim [a], Chul Oh Park [a], Ha Eun Choa [a], Seung Yong Lee [a,c], Myung Kyu Park [b], Hyegi Min [a,c,*], Kyu Hyoung Lee [a,**], Wooyoung Lee [a,**]

[a] Department of Materials Science and Engineering, Yonsei University, 50 Yonsei-ro, Seodaemun-gu, Seoul 03722, Republic of Korea
[b] Chem-bio Technology Center Team1, Agency for Defense Development, 160 Bugyuseong-daero 488 beon-gil, Yuseong-gu, Daejeon 34060, Republic of Korea
[c] KIURI Institute, Yonsei University, 50 Yonsei-ro, Seodaemun-gu, Seoul 03722, Republic of Korea

ARTICLE INFO

Keywords:
Chemical warfare agent
2-CEES
Gas sensor
Metal oxide semiconductor
Heterogeneous catalyst

ABSTRACT

We report the microwave-assisted synthesis of Au nanoparticles (NPs) anchored porous ZnO nanosheets (Au-ZnO NSs) and their application in the sensitive detection of 2-chloroethyl ethyl sulfide (2-CEES) vapors, which are a simulant of sulfur mustard chemical weapon. Upon microwave irradiation for < 1 min with an annealing, highly crystalline Au NPs with a narrow particle-size distribution (2.32 ± 0.40 nm) are densely formed on the surface of porous ZnO NSs, which increases the density of oxygen vacancies in the ZnO. Under the optimal working temperature (450 °C), the response of the Au-ZnO NS sensor was measured to be 787 for 10 ppm 2-CEES, which is ~14 times higher than that observed for the bare porous ZnO NSs-based sensor. Moreover, Au-ZnO NSs can detect 2-CEES gas even under high humidity (~80 %) benefiting from its high sensitivity. The highly reproducible sensing performance was verified by repeated sensing test (20 times for 12 h). According to gas screening data, the Au-ZnO NSs exhibited outstanding selectivity toward sulfide compounds due to the high Au-S affinity. In summary, we have successfully demonstrated a simple and facile approach to form the Au-ZnO heterostructure by microwave irradiation and enhanced the gas-sensing performance by inducing catalytic activity.

1. Introduction

Chemical warfare agents (CWAs) are poisonous chemical compounds that are severely harmful to living organisms, causing incapacitation, injury, and even death [1]. CWAs were mainly used in World War I and II, but have still been exploited in recent years, for examples, the terrorist attack on a Tokyo subway station in 1995 and the Syrian civil war in 2015. To cope with those threats, various techniques have been developed and utilized in the field for the precise sensing of CWAs, such as ion mobility spectrometry, flame photometry, infrared spectroscopy, photoionization detectors, Raman spectroscopy, and gas chromatography [2]. However, even though these techniques have outstanding sensing performance toward CWAs, human resources are required to operate most of these techniques in the middle of contaminated region, which may result in further victims. To avoid such risks, recently, remote-controlled robotic systems (i.e., drones) integrated with miniaturized sensing devices have attracted an increasing amount of interest [3]. However, the integration of conventional equipment into these systems is highly limited due to heavy weight, large size, and high-power consumption of the systems. Some devices can be miniaturized for facile integration, but their capability is limited, resulting in false positives originating from interfering compounds. To address these problems, a high-performing CWA-sensing device is required to be developed, which simultaneously possess outstanding sensing capability, compact size, light weight, and low power consumption.

For dozens of years, metal oxide semiconductors (MOSs) with a wide range of electron band gap energies have been used as electrochemical sensing materials of chemiresistors to analyze gaseous compounds [4,5]. In particular, the adsorption of vapor molecules on the oxide surface results in electron exchange via a series of chemical reactions. When

* Corresponding author at: Department of Materials Science and Engineering, Yonsei University, 50 Yonsei-ro, Seodaemun-gu, Seoul 03722, Republic of Korea.
** Corresponding authors.
E-mail addresses: hg1122@yonsei.ac.kr (H. Min), khlee2018@yonsei.ac.kr (K.H. Lee), wooyoung@yonsei.ac.kr (W. Lee).
[1] These authors contributed equally.

https://doi.org/10.1016/j.snb.2023.133726
Received 12 December 2022; Received in revised form 18 March 2023; Accepted 23 March 2023
Available online 24 March 2023

compared to conventional analytical methods, MOS-based gas sensors have advantages, such as compact size, low manufacturing cost, and low power consumption, due to the simplicity of the measurement system. Recently, the successful detection of dimethyl methylphosphonate (DMMP), 2-chloroethyl ethyl sulfide (2-CEES), the simulants in nerve agents (GB) and mustard gas (HD), has been reported using chemically modified MOS materials obtained via doping [6], morphology control [7], formation of heteroatomic junctions [8], and induction of catalytic reactions [9]. These approaches exhibit outstanding sensing performance toward the target gases, but production of undesired signals originating from interfering compounds remains a huge challenge. In another approach, a mixture of gases are passed through a gas separation system, such as a packed-bed column [10,11] or miniaturized gas chromatography column, to filter specific compounds or provide the retention time for gas transportation [12,13]. However, these techniques not only required large and complicate gas sampling systems but also applicable for compounds with different molecular weights, dipoles, and hydrophilicity, which is inappropriate when dozens of similar molecules are mixed.

Formation of heterostructures between noble metals and oxide sensing materials is an intrinsic approach to improve the selectivity because specific molecular structures have high affinity to metal surfaces. For example, Au is known to have an inert surface on the bulk scale, but it can be modified in nanoscale via ligand chemistry based on thiol (R-S-H) functional groups, forming various metal-organic molecule complexes, which result in self-assembled monolayers (SAM) [14,15]. Although the exact mechanisms of these interactions are still under debate, the thiol group (R-S-H) is known to be transformed into a thiyl radical (R-S•), which has a strong affinity toward Au (111) surface and is chemically trapped [14,16]. This Au–S interaction facilitates a wide range of applications, such as biosensing, molecular electronics, drug delivery, and nanopatterning [17–19]. Xu et al. recently reported the selective and sensitive detection of sulfide CWAs based on CuO/Au/Si arrays using surface-enhanced Raman spectroscopy (SERS) [20]. These results imply that the self-assembly of organic molecules on metal surfaces can also be applied in developing highly sensitive and selective electrochemical sensing devices.

Herein, we have demonstrated chemiresistive gas sensors based on the Au-ZnO heterostructure which enable outstanding sensing performance to 2-CEES, taking advantages of the strong Au-S interaction. Au NPs were synthesized and anchored on the surface of porous ZnO NSs using microwave irradiation which is able to homogeneous heating, uniform nucleation of precursors, and rapid crystal growth [21]. The detection of 2-CEES was carried out by using a compact size of microelectromechanical system (MEMS) through monitoring an electrical conductance during the chemical oxidation of 2-CEES in the presence of adsorbed oxygen ions on oxygen vacancies. We confirmed that the Au-ZnO NSs prepared via the microwave-assisted process not only exhibit the superior sensing performance than hydrothermally synthesized Au-ZnO NSs and bare porous ZnO NSs, but also maintain high response under humid conditions and during long-term measurements. Our study has experimentally demonstrated that the strong interactions between organic molecules and the noble metal surface contribute to enhance the sensitivity and selectivity simultaneously.

2. Experimental section

2.1. Starting materials

Zinc nitrate hexahydrate ($Zn(NO_3)_2{\cdot}6\ H_2O$) and urea ($CO(NH_2)_2$) were purchased from Sigma-Aldrich Co. Hydrogen tetrachloroaurate (III) hydrate ($HAuCl_4{\cdot}4\ H_2O$, Dajung Co.) was used as Au precursor. Ultrapure deionized (DI) water with a resistivity of 18 MΩ cm from Milli-Q was used for all solution preparations.

2.2. Synthesis of the Au-ZnO NSs

The synthesis procedure of the porous ZnO NSs was performed as described in our previous report [22]. Briefly, $Zn(NO_3)_2{\cdot}6\ H_2O$ was dissolved in a mixture of ethanol and water (1:2 v/v), and $CO(NH_2)_2$ (1:1 stoichiometry) was added with vigorous stirring to obtain a homogeneous mixture. After heating (180 °C for 24 h), drying (80 °C for 6 h), and annealing (550 °C for 5 h under an Ar atmosphere), porous ZnO NSs were obtained. To prepare the Au-ZnO NSs via microwave synthesis, 1 at % Au precursor ($HAuCl_4{\cdot}4\ H_2O$) and 0.8 g of ZnO NSs were mixed in 40 mL of DI water–ethanol. The mixture was placed in an alumina crucible and subsequently treated with microwave irradiation at a power of 1000 W for 1 min. A commercial microwave oven (Samsung, Model MS32K3513AK) with a frequency of 2.45 GHz was used. The resulting pink precipitate was collected and washed with DI water and absolute ethanol several times via centrifugation. Finally, Au-ZnO NSs were obtained after drying at 80 °C for 6 h followed by annealing at 300 °C for 3 h under an H_2 atmosphere.

As a control group to microwave-assisted synthesized samples, Au-ZnO NSs were also synthesized via the hydrothermal method. Here, 1 at% Au precursor ($HAuCl_4{\cdot}4\ H_2O$) and 0.8 g of ZnO NS were mixed in 40 mL of DI water–ethanol. The mixture was placed in the Teflon-lined autoclave and heated at 100 °C for 3 h. After the reactions, the product powder was collected by centrifugation and thorough washings with deionized water and ethanol. Finally, the powder was annealed at 300 °C for 3 h under an H_2 atmosphere.

2.3. Characterization

Scanning electron microscopy (SEM; JEOL-7800F, JEOL Ltd.) and transmission electron microscopy (TEM; JEM-F200, JEOL Ltd.) were used for visual characterization. High-angle annular dark-field scanning transmission electron microscopy (HAADF-STEM) and energy-dispersive X-ray spectroscopy (EDS) mapping were used to analyze the microstructure and elemental composition. The surface area was calculated using N_2 adsorption experiments and Brunauer–Emmett–-Teller analysis (BET, Autosorb-iQ 2ST/MP, Quantachrome). X-ray diffraction (XRD; Smart Lab, Rigaku) was carried out to characterize the phase and crystal structure using Cu-Kα irradiation ($\lambda = 1.5418$ Å). The chemical bonding states were investigated using X-ray photoelectron spectroscopy (XPS; K-alpha, Thermo Fisher Scientific Co.). All XPS profiles were calibrated using the C1s peak observed at 284.8 eV (C-C bond). Photoluminescence (PL) and Raman spectroscopy were conducted to study the lattice defects in the samples using excitation at 325 and 532 nm, respectively (LabRam Aramis and Horriba Jovin Yvon). The electronic structures of the bare porous ZnO NS and Au-ZnO NS were measured using ultraviolet photoelectron spectroscopy (UPS) and UV-Vis-NIR spectroscopy (V-650, JASCO Co.).

2.4. Evaluation of the gas-sensing performance

A commercially available MEMS (1 mm^2, RNS lab) consisting of a Joule heating circuit and drain/source electrode was used as a chemiresistive gas-sensing device. The synthesized porous ZnO NSs and Au-ZnO NSs were dispersed in ethanol to a concentration of 1 mg/mL via ultrasonication, respectively. 1 μL of the resulting dispersion was drop-casted several times onto the heated MEMS chip placed on a 100 °C hotplate. Each electrode was connected to a ceramic package via Au wire using a wire bonder (HB-05, TPT Wire Bonder GmbH & Co. KG). The heating circuit of the MEMS was connected to a direct current (DC) power supply (SDP30–5D, SMtechno), followed by heating to a specific temperature (200–500 °C) by controlling the Joule heating voltage (1.0–2.5 V). The resistance of the sensing materials was monitored using a digital source meter/source measurement unit (SMU, Keithley 2450, Keithley Instruments) under a constant voltage of 1 V. A standard gas cylinder containing 20 ppm 2-CEES balanced with N_2 was used as the

target gas. The gas flow rate was automatically regulated using a customized gas exposure system composed of mass flow controllers (MFCs), a gas chamber, and LabView software. The total gas flow rate was fixed at 1000 sccm during all measurements. At each measurement, sensors were stabilized at synthetic air for 1500 s to stabilize baseline resistance level, followed by being exposed to target gas for 300 s and synthetic air again for 1800 s to recover the resistance level. The 20 ppm 2-CEES gas was diluted with synthetic air at the desired ratio to prepare various concentrations of 2-CEES gas (1, 2, 5, 10, 15, and 20 ppm concentration). To measure the sensor response under humid conditions, moisturized air was prepared upon bubbling through DI water and mixing with dry synthetic air at a specific ratio (20, 40, 60, 80 % relative humidity).

3. Results and discussion

The experimental scheme of the synthesis of Au-ZnO NSs is illustrated in Fig. 1a. Briefly, ZnO NSs were successfully synthesized by a hydrothermal method in an autoclave chamber. To maximize the effective surface area for gas adsorption, the ZnO NSs were annealed at 550 °C under the Ar atmosphere to produce highly porous morphology (Fig. S1; see Supplementary material) [22]. As catalytic sites for gas adsorption and electrochemical reactions, Au NPs are introduced by irradiating microwave to homogeneous mixture of Au precursor and porous ZnO NSs. Then, the product was further annealed at H_2 atmosphere to achieve complete reduction and anchoring of Au NPs on the surface of porous ZnO NSs. The decorated Au NPs can be visualized in the TEM image using surface elemental analysis, which showed the Au NPs were densely distributed on the surface of a porous ZnO NS (Fig. 1b). We investigated how the microwave irradiation affected the formation of Au NPs, by comparing to the product without microwave treatment (Fig. S2; see Supplementary material). The result shows that sub-1-nm scale Au NPs were formed on the surface of porous ZnO NSs right after the microwave treatment due to the nucleation from Au precursors by rapid and homogeneous energy transfer. These Au particles and remaining un-reacted Au precursors were aggregated and tightly anchored on the surface of porous ZnO NSs when annealed at H_2 atmosphere for several hours. Further details were analyzed using HR-TEM to observe the shape, crystallinity, and particle-size distribution of the Au NPs. Figs. 1c and 1d show that the hemispherical shape of the Au NPs was clearly observed with a highly crystalline lattice structure. Fringe spacings of 0.26 and 0.239 nm correspond to the lattice planes of ZnO ($10\bar{1}0$) and Au (111), respectively, indicating the anchoring of the Au NPs onto the surface of porous ZnO NSs [23–25]. The Au NPs have a narrow particle-size distribution of 2.32 ± 0.40 nm (Fig. 1e). The well-organized Au NPs were attributed to the most energetically stable interface formed between Au (111) and ZnO ($10\bar{1}0$), which leads to the Au NPs being stably anchored onto the surface of porous ZnO NSs [26]. While the hydrothermally produced Au NPs in an autoclave chamber have a relatively large size (~50 nm) with low-density, microwave-assisted Au NPs had advantages in terms of simple experimental procedure, narrow particle-size distribution, and high-density decoration (Fig. S3; see Supplementary material). The studies on the heterostructure of Au-ZnO NS have been well established based on various approaches. As shown in Table 1, our simple and scalable procedure is a reducing-agent free process with fast reaction rate and facilitates the generation of highly dense and uniform sized Au NPs.

We further investigated the changes in the chemical states of the porous ZnO NS in the presence of the anchored Au NPs because the

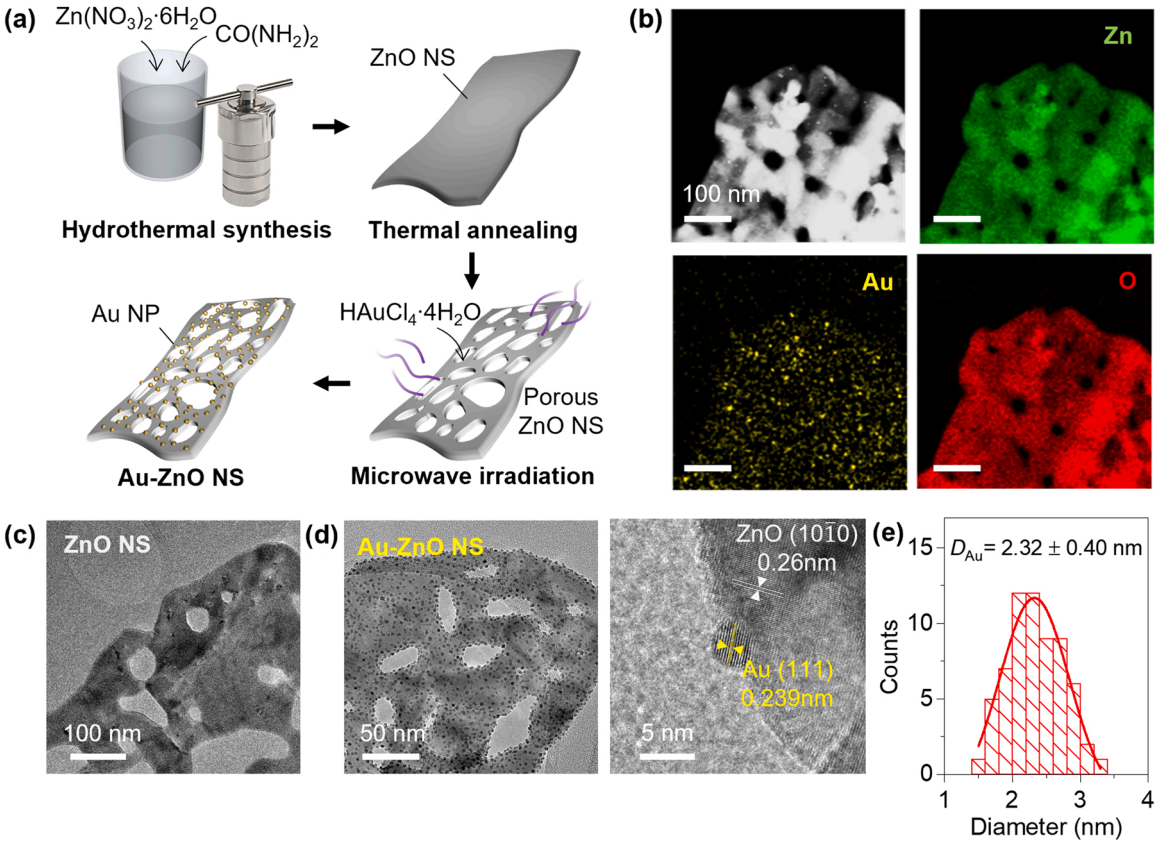

Fig. 1. (a) Schematic of Au nanoparticles–anchored porous ZnO nanosheet (Au-ZnO NS) fabrication process. (b) Surface elemental analysis of the Au-ZnO NS by using energy-dispersive X-ray spectroscopy (EDS). Images of phase contrast (upper left), zinc (upper right), gold (bottom left), and oxygen composition (bottom right). Picture of (c) bare porous ZnO NS and (d) Au-ZnO NS obtained from high-resolution transmission electron microscopy (HR-TEM). (e) Size-distribution of Au nanoparticles anchored onto the surface of porous ZnO NSs.

Table 1
Previous studies on Au/ZnO heterostructures.

Morphology of ZnO	Synthesis method	Reagent	Particle size	Application	Reference
ladder-like structure	Annealing (H_2)	$HAuCl_4$•4 H_2O	Au single atom	Gas sensor	[27]
Nano-rod	Chemical method	$HAuCl_4$·3 H_2O, $Na_3C_6H_5O_7$·2 H_2O	~15 nm	UV photodetector	[28]
Cylindrical structure	Hydrothermal	$NaBH_4$, $HAuCl_4$	~4 nm	Photocatalyst	[29]
Nano-wire	Deposition–precipitation method	$HAuCl_4$ Na_2CO_3	6.3 ± 3 nm	Catalytic oxidation	[30]
Porous nano-sheet	Microwave & annealing (H_2)	$HAuCl_4$•4 H_2O	2.32 ± 0.40 nm	Gas sensor	This study

interfacial junction between the noble metal and oxide support acts as an 'electron exchange window', inducing structural defects in the oxide lattice. To clarify the effect of the microwave irradiation, we also gathered the XRD spectrum of microwave treated porous ZnO NSs without Au precursors. Fig. 2a shows the XRD patterns obtained for the bare porous ZnO NSs and Au-ZnO NSs, which clearly exhibit the single phase of the hexagonal wurtzite ZnO phase (JCPDS No. 36–1451). According to the patterns, no impurity phase was detected, but the (100), (002), and (101) diffraction peaks of microwave-treated porous ZnO NSs and Au-ZnO NSs were shifted to a higher angle compared to those observed for the bare porous ZnO NSs (Fig. 2b). The shift in the XRD peaks can be attributed to the stress of the unit cell in the crystal structure due to the presence of ions with abundant oxygen vacancy defects at the porous ZnO NSs interface of oriented attachments [31]. In other words, electromagnetic field of the microwave induces dipolar polarization of ZnO lattice, so the energy transforms to heat producing defect sites [32]. Moreover, full width at half maximum (FWHM) of peaks appeared to be broaden after anchoring of Au NPs, which means the Au NPs weaken the crystallinity of ZnO lattice structure by forming Au-O-Zn heteroatomic junction interfaces [33]. The change in the ZnO lattice structure was further studied by the analysis of chemical bonding states using the XPS with respect to Zn, O, and Au (Fig. 2c–e). As shown in Fig. 2c, Zn $2p_{1/2}$ and $2p_{3/2}$ states were clearly observed at 1044.22 and 1021.12 eV, respectively, which denote the Zn-O bonding state. The

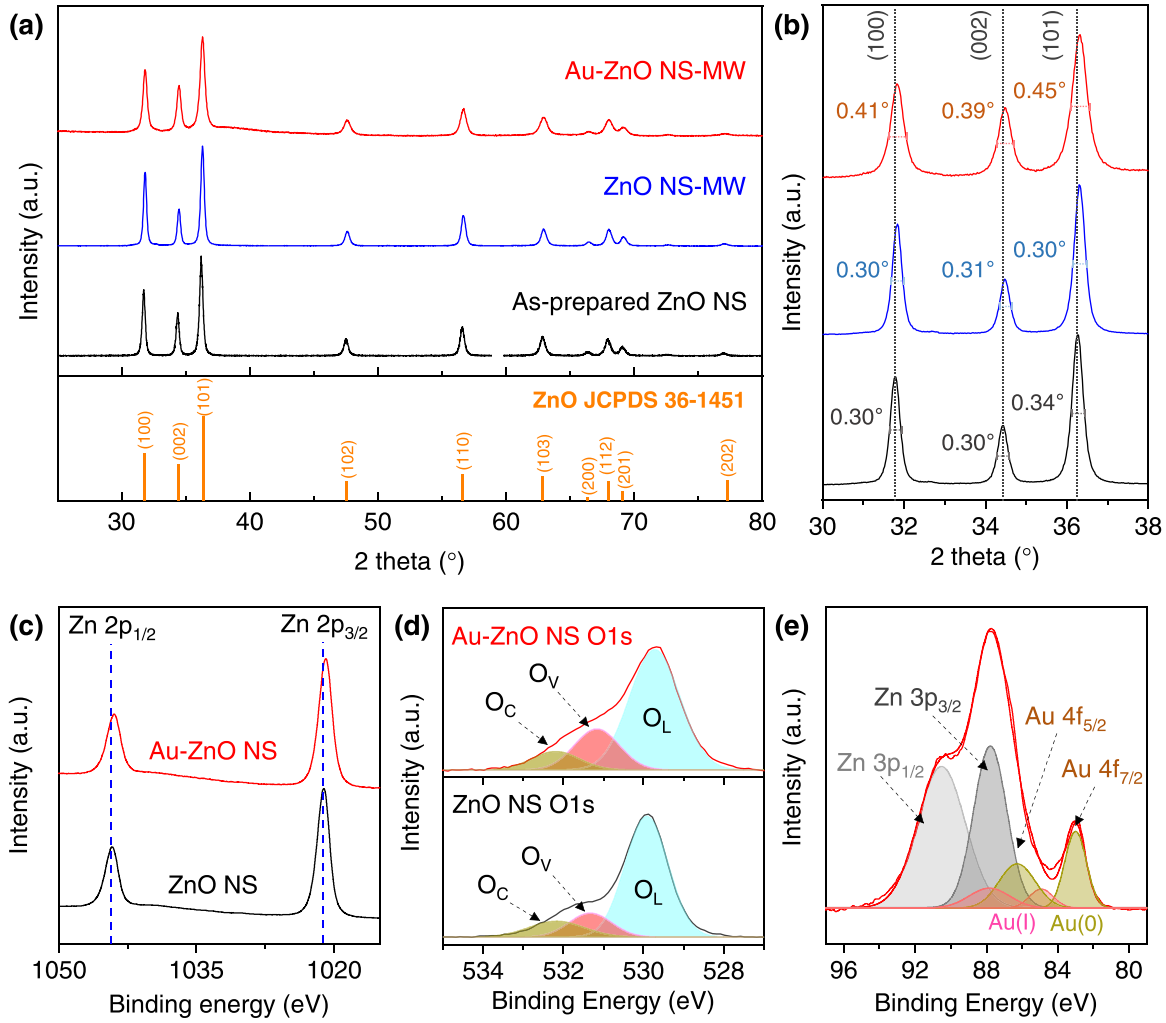

Fig. 2. (a) Crystallographic analysis of Au-ZnO NS and bare porous ZnO NS by using the X-ray diffraction (XRD). (b) Shift of ZnO lattice position after microwave irradiation and peak broadening after anchoring Au NPs. (c-e) Analysis of chemical bonding states of bare porous ZnO NS and Au-ZnO NS obtained from high-resolution X-ray photoelectron spectroscopy (XPS). (c) Binding energy of Zn before and after anchoring Au NPs. (d) Oxygen binding states on bare porous ZnO NS and Au-ZnO NS. O_L, O_V, and O_C denotes lattice oxygen, deficient oxygen, and chemisorbed oxygen, respectively. (e) Binding states of anchored Au NPs onto the surface of porous ZnO Ns.

binding energy value of the Zn 2p state in Au-ZnO NSs was also slightly downshifted by ~0.31 eV when compared to the bare porous ZnO NSs, which was ascribed to an enhancement in the electron density around the Zn atoms [34,35]. The effect of anchored Au NPs on Zn-O bonding states was also confirmed based on the deconvoluted O1s spectra (Fig. 2d); Zn-O lattice oxygen (O_L ~530 eV), vacant oxygen (O_V ~531 eV), and chemisorbed oxygen (O_C ~532 eV). The changes in the oxygen states of the bare porous ZnO NSs and Au-ZnO NSs are summarized in Table 2. Remarkably, the O_V ratio was higher after anchoring the Au NPs. A previous density-functional theory (DFT) study has reported that when a noble metal is in close contact with a metal oxide surface, the metal not only significantly lowers the energy required to produce oxygen vacancies, but also stabilizes the vacant sites because noble metal clusters tend to capture more electron density [33]. In other words, more oxygen vacancies are distributed at the peripheral sites of noble metal clusters because an oxygen vacancy acts as an electron donor. In our system, the hemispherical Au NPs are densely anchored on the surface of porous ZnO NSs, which provides ideal conditions for the formation of oxygen vacancies. Finally, the binding energies of Zn 3p and Au 4f observed for the Au-ZnO NS were analyzed and deconvoluted into several components corresponding to Zn $3p_{1/2}$ (90.51 eV), Zn $3p_{3/2}$ (87.77 eV), Au $4f_{5/2}$ (86.99 eV), and Au $4f_{7/2}$ (83.02 eV) (Fig. 2e). The Au 4f signals were also deconvoluted into ionic (Au^+) and metallic phase (Au^0), which implied the existence of Au-O-Zn interfaces. Notably, the binding energies of Au $4f_{5/2}$ and Au $4f_{7/2}$ were downshifted as much as 0.72 and 0.98 eV, respectively when compared to bulk Au (Au $4f_{5/2}$ = 87.71 and Au $4f_{7/2}$ = 84.00 eV) [23,24,36–38]. The shift of the Au signals also verified the existence of a large electron density around the Au atoms, originating from the oxygen vacancies formed in the ZnO lattice. To sum up, the interfacial interaction between the Au NPs and ZnO has a significant effect on the formation of oxygen vacancies due to the charge exchange.

The generation of defects in Au-ZnO NSs was also confirmed using Raman spectroscopy. The photoluminescence (PL) spectra obtained from the bare porous ZnO NSs and Au-ZnO NSs were compared because PL measurement is closely related to the degree of defects corresponding to the O_V in the MOS (Fig. 3a) [39]. Both the signal intensity and accumulated signal area appear to increase in the Au-ZnO NSs, which indicates that the degree of defects was increased. We also measured the Raman spectra of the bare porous ZnO NSs and Au-ZnO NSs at an excitation laser wavelength of 532 nm. In case of the bare porous ZnO NSs, the wurtzite phase vibrational mode of ZnO was mainly observed at 438 cm^{-1} [E_2(high)]. The overall Raman shift in Au-ZnO NSs in the range of 100–800 cm^{-1} exhibited a slight red-shift due to the weakened Zn-O bonding, which matches the decrease in the lattice parameter observed in our XRD analysis (Fig. S4, see Supplementary material). It has been observed that the peak position shifts toward a lower wavenumber, indicating the occurrence of structural changes [40]. When compared to the bare porous ZnO NSs, the broad and weak peak observed at ~438 cm^{-1} [E_2(high)] can also be assigned to the lower crystal quality of the P63mc symmetry of the wurtzite structure due to the higher density of defects and stress in the Au-ZnO NSs. In addition, the E_1(LO) phonon mode observed at ~581 cm^{-1} represents the defects in ZnO lattice, such as interstitial defects (Zn_i) or O_V. This peak was deconvoluted using Lorentz fitting with the A_1(LO) peak at ~557 cm^{-1}, which was related to the O_V defects (Fig. 3b) [41,42]. In consequence, Au NPs anchoring affects the ZnO lattice structure and produces a lot of defect sites.

Table 2
Binding states of the oxygen species observed using XPS.

Sample	O_L (eV, %)	O_V (eV, %)	O_C (eV, %)
Bare porous ZnO NSs	529.92 (73.32 %)	531.32 (14.43 %)	532.17 (12.25 %)
Au-ZnO NSs	529.71 (69.01 %)	531.16 (21.02 %)	532.18 (9.97 %)

Finally, we analyzed the change of band structure after anchoring of Au NPs. The work function (φ) and Fermi level (E_F) of the bare porous ZnO NS and Au-ZnO NS were measured using the UPS (Fig. 4a–b). The band gap energy (E_g) was calculated by measuring the edge of the absorption profile, Tauc-plot, using UV–vis NIR spectroscopy (Fig. 4c). The E_F of Au-ZnO NS (2.03 eV) was slightly higher than that of bare porous ZnO NS (1.96 eV), implying the electron doping effect from by oxygen vacancies and strong *n*-type transport characteristics [35,43]. The φ values were measured to be 3.22 and 3.01 eV for the bare porous ZnO NS and Au-ZnO NS, respectively, which indicates that electrons can be emitted easier from the Au-ZnO NS than bare porous ZnO NS. Furthermore, the E_g of the Au-ZnO NS (2.88 eV) also reduced compared to the bare porous ZnO NS (3.00 eV), which is attributed to the high level of oxygen vacancies creating an impurity energy level near the valence band energy level [44]. An energy band diagram was expressed in Fig. 4d based on these measurements. The modulated band structure of the Au-ZnO NS clearly shows that the anchored Au NPs create high-density surface electrons from the oxygen vacancy, which result in a strong *n*-type configuration.

The gas-sensing properties of Au-ZnO NSs were investigated because the degree of oxygen vacancies is one of the principal factors determining the sensing performance [45]. Many studies have reported that the sensitivity is dramatically enhanced by increasing the number of oxygen vacancies through modifying materials via doping [46], surface chemistry [47], and size control [48]. In this study, we verified an increase in the number of oxygen vacancies by forming noble metal/oxide heterostructure, so we expected that Au-ZnO NSs exhibited superior sensing properties than those of the bare porous ZnO NSs. We fabricated a MEMS-based chemiresistive gas sensor and conducted gas exposure experiments in a customized gas chamber system (Fig. S5; see Supplementary material). Briefly, the bare porous ZnO NSs and Au-ZnO NSs were dispersed in ethanol and drop-casted onto a heated MEMS until the drain/source electrode was connected by the sensing materials enough. The operating temperature of the gas sensor was controlled via Joule heating upon applying a voltage to the heat-inducing circuit. The generated heat was rapidly transferred to the sensing materials on the measurement electrode within a few seconds. Because the baseline resistance and signal amplitude are susceptible to the temperature, we normalized the sensor response using Eq. (1):

$$Response = \frac{R_a - R_g}{R_g} = \frac{\Delta R}{R_g} \quad (1)$$

where R_a and R_g are the 10 s average resistance measured in the baseline air atmosphere and a minimum resistance value upon exposure to 2-CEES, respectively. We calculated the changes in the electrical conductance upon gas exposure.

The electronic properties of the deposited sensing materials were characterized before performing the gas exposure experiments. We found that bare porous ZnO NS and Au-ZnO NS exhibited different baseline resistance trends depending on the Joule heating temperature (Fig. S6; see Supplementary material). In general, when a MOS is heated up, the electrons in the valence band are excited to the conduction band, which increases the electrical conductivity. This phenomenon was observed in the bare porous ZnO NSs-based sensor when the temperature was increased from 200° to 500 °C at 50 °C intervals. However, in contrast, the resistance level of the Au-ZnO NSs-based sensor gradually decreased in the lower temperature range (<250 °C) but increased at temperatures range over 300 °C. This disparity can be interpreted as difference in potential energy barrier on the conducting pathway, which resulted from an electron depletion layer (EDL) [49]. Chemisorbed oxygen molecules are known to be dissociated and ionized to O^- at 100 – 300 °C and begin to be further ionize to O^{2-} at higher temperature by

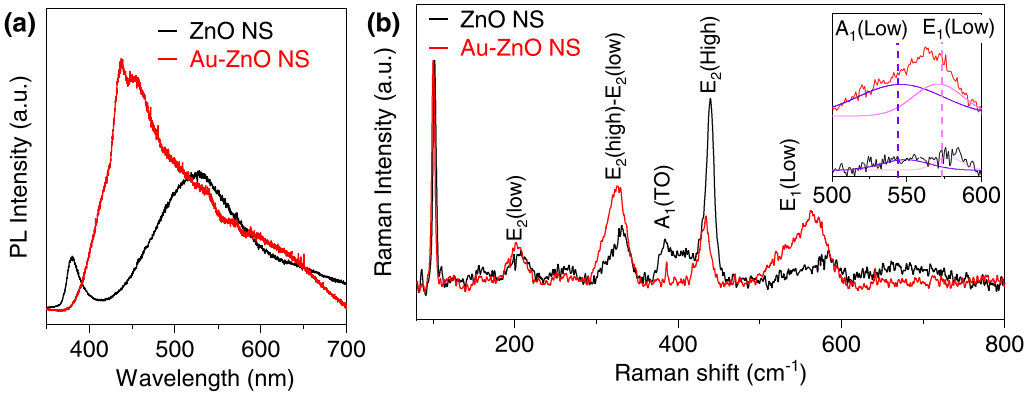

Fig. 3. (a) Photoluminescence (PL) measurement of bare porous ZnO NS and Au-ZnO NS. (b) Observation of Raman shift after anchoring Au NPs. Inset shows the phonon vibrational peak at ~580 cm^{-1}, deconvoluted by Lorentz distribution of two phonon modes, A_1 (low) and E_1 (low).

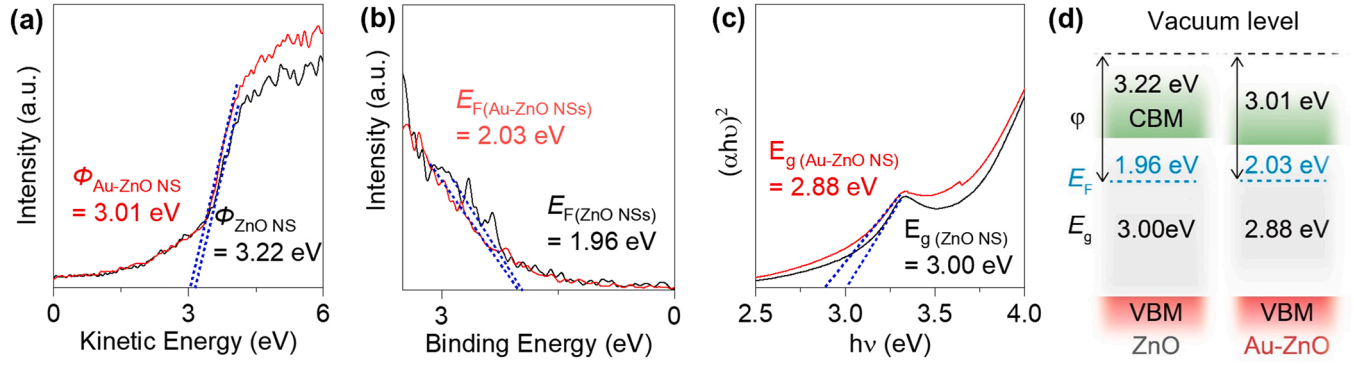

Fig. 4. Analysis of band gap structure of bare porous ZnO NS and Au-ZnO NS. (a) Kinetic energy of ejected electrons and (b) binding energy of electrons measured by ultraviolet photoelectron spectroscopy (UPS). (c) Measurement of band gap energy calculated from Tauc-plot obtained by UV–vis-NIR spectroscopy. (d) Estimated band structures of the bare porous ZnO NS and Au-ZnO NS.

getting electrons from oxygen vacancies [50,51]. During the process, the EDL is formed at the surface of oxide because the electrons of the oxide is transferred to the oxygen atoms [45]. In other words, the more oxygen vacancies that exist in the metal oxide surface, the more electrons are drawn from the conduction band of the oxide, which produces a thicker depleted electron layer, producing a higher potential barrier. We previously confirmed that Au NPs induced a lot of oxygen vacancies on the lattice of ZnO NS due to high electron charge density. We can deduce that Au-ZnO NS has much thicker EDL than bare porous ZnO NS. Especially, the resistance of Au-ZnO NS starts to increase from 300° to 400°C, which means the ionization of oxygen molecules is fostered by the catalytic effect of anchored Au NPs under this temperature region. In consequence, mobile charge carriers in a NS cannot be transported freely into other NSs because of this energy barrier. Considering the decrement of resistance level even at the high temperature, the energy barrier in the bare ZnO NS seemed much weaker than that of Au-ZnO NS. This trend is attributed to the low number of oxygen vacancies, which provided less active sites for oxygen ionosorption.

We measured sensor response to 2-CEES, which is a simulant of the sulfur-mustard CWA, to analyze how the Au NPs contribute to sensing performance. Previous studies have reported the outstanding sensitive and selective detection of sulfur compounds using the SERS effect of Au NPs [20,52–54]. Heterogeneous catalysis studies have also reported that oxidation reaction via the Mars-van-Krevelen mechanism occurs between the adsorbed molecules on noble metal species and peripheral oxygen around the anchored metal cluster [55,56]. Therefore, we hypothesized that the Au-ZnO NS also have sensitivity toward sulfide compounds by high catalytic activity. To verify our hypothesis, we conducted a gas-sensing experiment using sulfur compounds. Initially, we performed temperature-dependent gas-sensing tests to determine the optimal working temperature of the Au-ZnO NS for sensing 2-CEES (Fig. 5a). The fabricated gas sensors were exposed to 10 ppm 2-CEES using a customized gas exposure system after stabilizing the baseline resistance. For *n*-type ZnO-based gas sensor, the detection of 2-CEES appeared as an abrupt decrease in the resistivity. The measured sensor response is shown in Fig. 5b. This result shows that both bare porous ZnO NS and Au-ZnO NS cannot detect 2-CEES gas at 200 °C, but they exhibit different response trends at higher temperatures. While the response of the bare porous ZnO NS-based sensor was gradually increased from 250° to 500 °C, whereas the response of Au-ZnO NS-based gas sensor appeared to be a pyramidal profile with a maximum response at 450 °C. The response of the bare porous ZnO NS-based sensor was comparable to or slightly higher than that of the Au-ZnO NS-based gas sensor in the low-temperature range (<300 °C). However, the response of the Au-ZnO NS-based sensor begins to be dramatically enhanced above 300 °C (1.168 ppm^{-1}/°C for 350–400 °C and 0.232 ppm^{-1}/°C for 400–450 °C), which exhibits a ~14 times higher value (≈787) than that observed for the bare porous ZnO NS-based sensor (≈56) at 450 °C. Here, the response and recovery time of Au-ZnO NS were estimated as 27 s and 822 s, respectively, similar to values obtained by the bare ZnO NS (36 s and 824 s). As the control group of the microwave-assisted synthesized Au-ZnO NS, the hydrothermally prepared Au-ZnO NS were tested, but we could not observe any sensing enhancement, presumably due to the low density, large size, and non-anchored Au NPs on the metal oxide (Fig. S7; see Supplementary material). We further investigated the effect of Au contents on the gas sensing performances by preparing different quantities (0.5 and 2 at %) of Au-ZnO NS samples (Fig. S8; see Supplementary material). Among

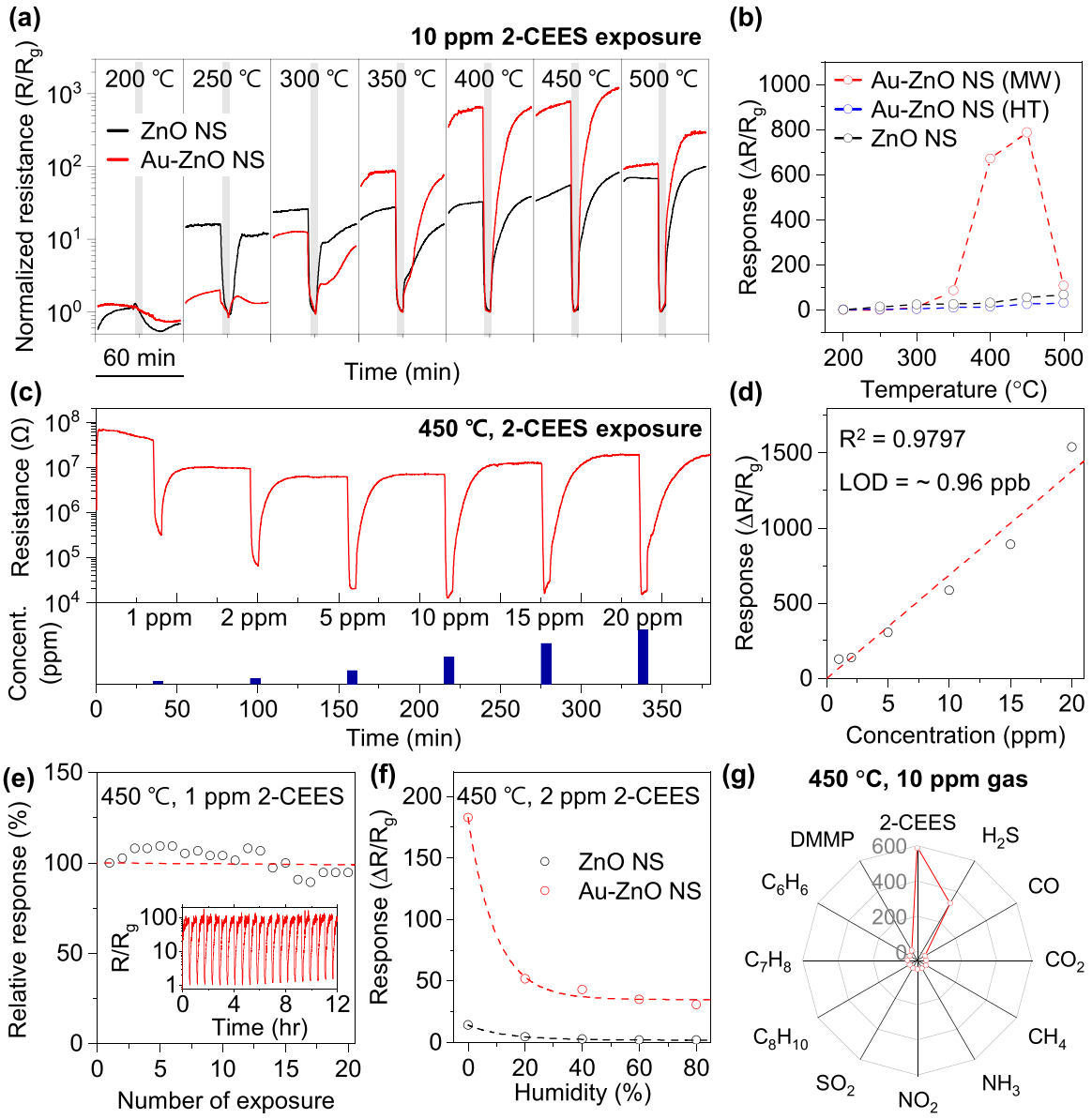

Fig. 5. Evaluation of gas sensing performances of bare ZnO NS and Au-ZnO NS. (a-b) Temperature-dependent normalized resistance curve upon exposure to 10 ppm 2-CEES (a) and calculated response (b) for microwave (MW) -assisted synthesized Au-ZnO NS, hydrothermally (HT) synthesized Au-ZnO NS, and bare ZnO NS. (c-d) Gas concentration-dependent gas sensing performances of Au-ZnO NS gas sensor. (c) The resistance curve of the Au-ZnO NS sensor under exposed to various concentration of 2-CEES gas, and calculated response (d). (e) Evaluating reproducibility of sensing performances by repeating gas exposure 20 times for 12 hr. (f) Measurement of gas sensing performances of Au-ZnO NS and bare porous ZnO NS sensors under various humidity condition. (g) Sensing selectivity of Au-ZnO NS gas sensors to various gaseous compounds.

those, the 1 at% Au content showed the highest response, which was determined to be the optimized condition for gas sensing.

Through the measurement, we could observe the correlation between the baseline resistance level and the sensor response. As previously described, anchored Au NPs promote the formation of oxygen vacancies, producing a thicker electron depletion layer and decreased the electrical conductivity. Under these conditions, 2-CEES has a greater chance of reacting with ionized oxygen on oxygen vacancies, facilitating the electron exchange between 2-CEES and the metal oxide, which result in a dramatic change in resistance. This mechanism seemed like to be applicable at temperatures > 300 °C when the resistance of the Au-ZnO NS started to increase. On the other hand, the gas detection mechanism of the Au-ZnO NS will be similar to the bare porous ZnO NS in the low working temperature range (<300 °C), where the catalytic effect was insignificant. Our BET results verified that the pore volume was reduced after anchoring of Au NPs onto the surface of porous ZnO NS, which means that some of the active sites of the porous ZnO NS were covered with Au NPs (Fig. S9; see Supplementary material). These reduced active sites cause the low response of the Au-ZnO NS in the low-temperature range (<300 °C). Meanwhile, when the temperature is > 450 °C, the response is significantly reduced (−1.358 ppm^{-1}/°C), presumably due to the low thermal stability of the Au NPs [57,58], sublimation of the porous ZnO NS structure [59], and excess ionization of oxygen atoms, which affect the stoichiometry of chemical oxidation [51].

After determining the optimal temperature, we further performed a quantitative analysis depending on gas concentration. For the experiment, various concentrations of the 2-CEES gas (1, 2, 5, 10, 15, and 20 ppm) were prepared by diluting a 20 ppm 2-CEES standard gas with synthetic air using MFCs. The sensor was exposed to target gas from a low to high concentration one sequentially, and the sensor resistance was measured (Fig. 5c). The amplitude of the sensor signal gradually increases under the higher concentration of 2-CEES gas. Since the

balancing gas of 2-CEES gas was N_2 gas, sensor response could be affected by the difference in the O_2 ratio in the balancing gas. To clarify the effect of the O_2 portion, we investigated resistance level shifts at various O_2 contents in the carrier gas (Fig. S10; see Supplementary material). According to the results, we confirmed that the impact of the O_2 contents was almost negligible except for the case of the absence of O_2 (0%) in the balancing gas. In other words, the sensor response to the 20 ppm 2-CEES seemed to slightly overestimated. We plotted the sensor response obtained for each concentration and found that the least-squares regression of linear fitting was highly matched with the data ($R^2 = 0.9797$) (Fig. 5d). Based on the fitting curve, the sensitivity of the Au-ZnO NS-based gas sensor was calculated to be ~68.81 ppm^{-1}. The limit of detection (LOD) of the Au-ZnO NS sensor was estimated to be 0.96 ppb calculated by three times of standard deviation extracted from baseline resistance. We randomly tested sensitivity of 16 sensors toward 1 ppm 2-CEES gas to figure out the yield of the high-performance sensors. According to the interquartile range (IQR) results, 15 of 16 sensors (1 outlier) showed a high response (85.31 ± 37.20 ppm^{-1}) to 2-CEES gas, which was a comparable value to our fitting curve (Fig. S11, see Supplementary material). Then, the reproducibility of the sensing capability was estimated by exposing the sensor to 1 ppm 2-CEES gas 20 times for 12 h (Fig. 5e and S12; see Supplementary material). Although the sensor was exposed to the harsh condition (450 °C) for 12 hr, the baseline resistance was almost constant, showing stable sensing responses. When each response was normalized to the initial response, the linear regression fitting curve shows a slope of 5×10^{-4}, implying that the sensor was highly reproducible despite of repeating measurements for a long-term. Table 3 summarizes the reported sensing properties related to 2-CEES detection. Although our previous study on quantum dot (QD) materials exhibit a higher sensing response than this work, QD materials suffered from poor stability after exposure to high-temperature conditions [48]. Our sensors have proven outstanding sensing performances in terms of maintaining their high sensitivity for a long-term measurement.

To confirm the validity of Au-ZnO NS for detecting CWA gas sensor, the humidity-dependent capability should be verified because CWAs are usually utilized in an outdoor environment. One of the challenging issues in MOS-based gas sensors is the poisoning of the sensing materials by atmospheric moisture due to the competitive adsorption of water molecules on the metal oxide surface [65]. Many approaches have been developed to minimize water poisoning, such as the integration of hydrophilic packed-bed columns [10], hydrophobic layer deposition [66], surface functionalization of oxides with humidity-resistant hydrophobic polymers [67], and coating metal-organic frameworks [68]. Although these methods are effective against moisture poisoning, the coated functional materials limit the operating conditions of the sensing materials because the oxidation of complex molecules usually requires high temperature. Therefore, improving sensor sensitivity is an important factor in overcoming water-poisoning effects. To evaluate the sensing performance under a variety of humid conditions, we controlled the humidity level by diluting water-saturated air with dry one. The concentration of 2-CEES gas was fixed at 2 ppm and we measured the sensing performance at 0%, 20%, 40%, 60%, and 80% humidity (Fig. 5f and S13; see Supplementary material). In the presence of 20 % humidity, both the Au-ZnO NS-based and bare porous ZnO NS-based sensors were significantly poisoned by moisture and the amplitude of the response was reduced to 30 % (52 for Au-ZnO NS and 4.71 for bare porous ZnO NS) when compared to those under dry conditions (183 for Au-ZnO NS and 14.25 for bare porous ZnO NS). The response was further reduced at the higher humidity (80 %) to 31 for Au-ZnO NS and 2.18 for bare porous ZnO NS, in which the Au-ZnO NS exhibited an ~15 times higher response than the bare porous ZnO NS. Based on the results, we approximately quantified the effect of relative humidity to the sensitivity of Au-ZnO NS gas sensor; the sensitivity decreased by 3.275 ppm^{-1}/RH% from 0 % to 20 % and 0.175 ppm^{-1}/RH% from 20 % to 80 %. Although the sensing capability was significantly deteriorated by moisture, the Au-ZnO NS still exhibited a high response toward 2-CEES vapor due to the dramatic enhancement in the sensitivity by the catalytic effect of the anchored Au NPs.

To figure out the false-positive malfunction of the sensor to interfering gases, we investigated the sensing selectivity of the Au-ZnO NS with respect to commonly observed carbon oxidation compounds (CO and CO_2), hydrocarbons (CH_4, benzene (C_6H_6), toluene (C_7H_8), and xylene (C_8H_{10})), nitrogen compounds (NH_3 and NO_2), sulfur compounds (H_2S and SO_2), and the simulant of the nerve agent DMMP (Fig. 5 g and S14; see Supplementary material). Gas concentration was fixed at 10 ppm. The highest response was observed for H_2S (324), followed by DMMP (14.7), CH_4 (6.85), C_7H_8 (6), and NH_3 (1.67). The Au-ZnO NS-based sensor has outstanding selectivity toward 2-CEES gas except H_2S, considering that the response to 10 ppm 2-CEES was ~587. This high selectivity toward sulfur compounds can be explained by the high interaction affinity between the gold surface and sulfur atoms. Especially, when the sulfhydryl group is deprotonated, a thiyl radical (R-S•) is created forming covalent interaction with Au surface. Even though the radical is not created, the thiol group (R-SH) has coordination-type bond interaction with Au surfaces through lone pair electrons at the sulfur [14]. The 2-CEES molecules are known to dissociate into two radicals at high temperature and terminate with a sulfur radical [69]. This can actively interact with the Au (111) surface, so that the molecule can be reacted efficiently with the lattice oxygen [14]. In the case of SO_2, sulfur is already fully oxidized, thus no oxidation can occur on the oxide surface.

The gas-sensing mechanism is depicted in Fig. 6 based on the sensing results. For MOS-based gas sensors, the gas sensing reaction occurs in two-step: 1) adsorption, dissociation, and ionization of oxygen molecules on the oxide surface and 2) oxidation reactions of the target molecule with ionized oxygen. For the first step, when the bare porous ZnO NS is exposed to air, the gas-phase oxygen ($O_{2(g)}$) diffuses to the metal oxide surface and is physically adsorbed ($O_{2(ads)}$). As temperature increases, these adsorbed oxygen molecules receive electrons from the oxide and are chemisorbed ($O^-_{2(ads)}$). On high-temperature oxide surfaces (>300 °C), the oxygen molecules dissociate and ionize into $O^-_{(ads)}$ and

Table 3
Previous studies on 2-CEES detection gas sensors.

Sensing material	Operating temperature (°C)	Gas concentration (ppm)	Response ($\Delta R/R_0$)	Response time (s)	Recovery time (s)	Reference
Au-ZnO NS	450	10	787	27	822	This study
WO_3/WS_2 heterostructure	240	5.7	0.81	20	55	[60]
Al-doped ZnO QD	450	20	5393	3	406	[48]
ZnO QD	450	20	4614	3	207	[48]
Al-doped ZnO NP	500	20	954	2	127	[61]
ZnO NP	500	20	344	6	165	[61]
Sm_2O_3 doped SnO_2 NP	200	10	540	40	20	[62]
SnO_2 NP	250	10	180	50	20	[62]
Ru-$CdSnO_3$ thin film	350	4	62	5	185	[63]
Pt-$CdSnO_3$ thin film	250	4	59	30	300	[64]
$CdSnO_3$ thin film	350	4	12	2	75	[64]

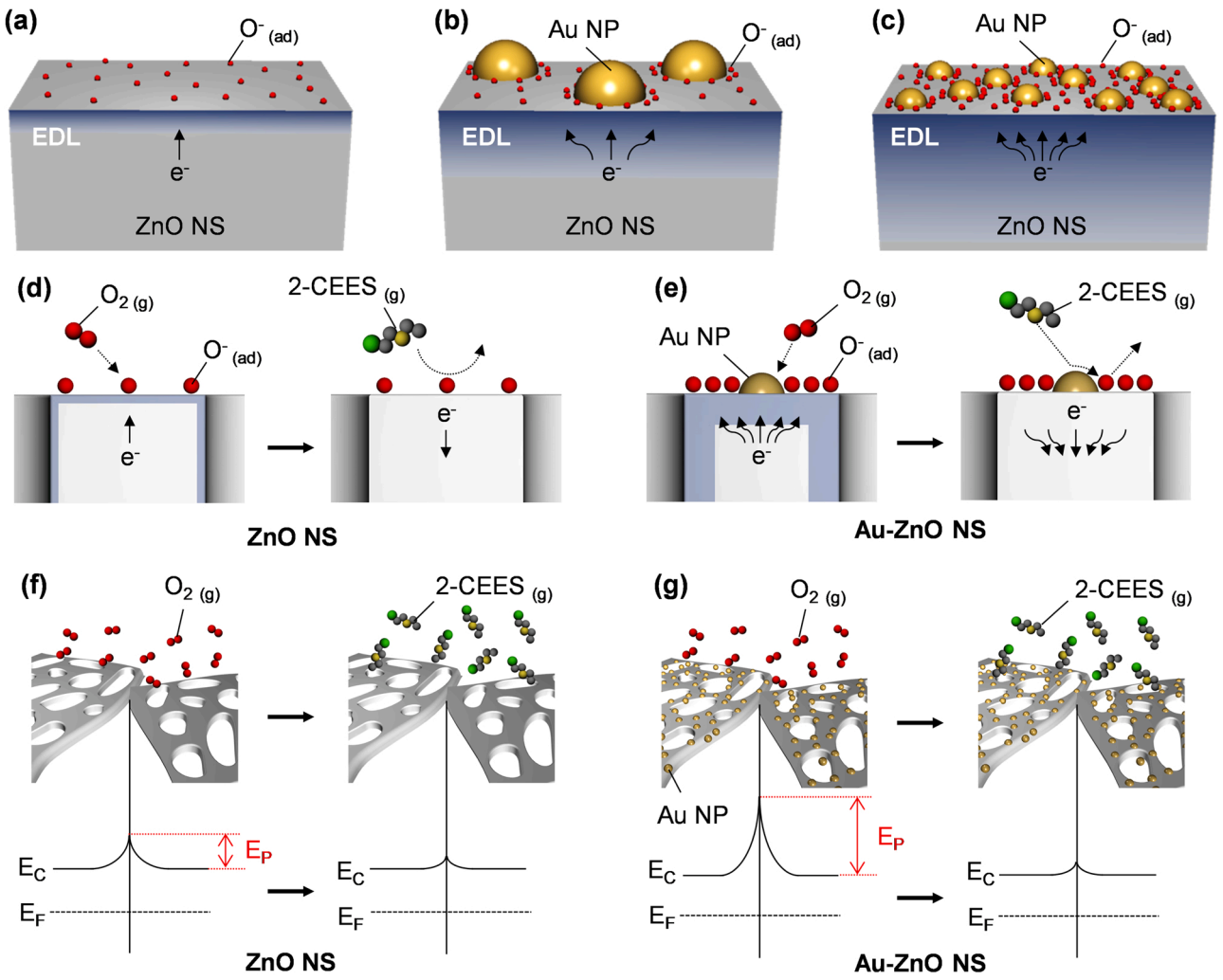

Fig. 6. Illustration of gas sensing mechanisms. Formation of electron depletion layer (EDL, blue) by oxygen ionization depending on the anchoring states of Au NPs, (a) without Au NPs, (b) rare density of large Au NPs, and (c) densely anchored nanoscale Au NPs. (d) Gas sensing mechanisms on the bare porous ZnO NS. The 2-CEES molecules react with ionized oxygen atoms adsorbed on the oxide surface. (e) Gas sensing on Au-ZnO NS surface. The Au NPs provide efficient reaction pathway for 2-CEES oxidation taking advantages of the gold-sulfur interaction and the Mars-van-Krevelen mechanism. Change of potential barrier (E_P) of (f) bare porous ZnO NS and (g) Au-ZnO NS. The Au-ZnO NS has a large E_P than that of bare porous ZnO NS due to the thick EDL. The E_P decreases after reacting with 2-CEES molecules.

$O^{2-}_{(ads)}$ by gaining further electrons from the oxygen vacancies. The kinetics of the oxygen ionization on the metal oxide surface can be described using the following equations [51]:

$$O_{2(g)} \rightarrow O_{2(ads)} \quad (2)$$

$$O_{2(ads)} + e^- \rightarrow {O_2}^-{}_{(ads)} \quad (3)$$

$${O_2}^-{}_{(ads)} + e^- \rightarrow 2{O}^-{}_{(ads)} \quad (4)$$

$${O}^-{}_{(ads)} + e^- \rightarrow {O}^{2-}{}_{(ads)} \quad (5)$$

During these processes, an EDL is formed on the oxide surface due to electron consumption to ionize the oxygen atoms. Here, the depth of EDL can be modulated in the presence of anchored Au NPs (Fig. 6a-c). According to several studies on the heterogeneous catalyst, supported noble metal NPs have a role as an electronic and chemical sensitizer to modulate EDL and resistance levels [70–73]. The electronic sensitization usually occurs due to the work function differences between contacting materials, in this experiment, Au (5. 1 eV) and ZnO NS (3.22 eV, obtained from the UPS measurement). Here, when Au nanoparticles come into contact with the ZnO surface, Schottky junctions are formed at interfaces, which causes electron transfer from the ZnO to Au and bending of the energy band structure. These electrons help oxygen molecules to diffuse and be ionosorbed onto the sensing materials effectively, causing the thick EDL. In terms of chemical sensitization, also known as the spillover effect, the anchoring of Au NPs on ZnO forms a bunch of defect sites with high electron density, which are also effective active sites for oxygen breakage. In the previous section, our structural characterization has verified the formation of these defect sites, oxygen vacancies. The Au-ZnO NS have a much higher oxygen deficiency than that of the bare porous ZnO NS due to the high charge density of noble metals. Most oxygen vacancies are located at the perimeter of Au NPs, so oxygen molecules are ionized on those sites [33]. Since more electrons are taken from the oxide to oxygen, a thicker EDL is formed in the presence of anchored Au NPs, which means the density and size of the Au NPs determine how many electrons are consumed. For instance, the densely anchored small Au NPs induce oxygen ionization much easier than rarely anchored large Au NPs due to the enormous amount of peripheral vacancy sites around Au clusters. In the case of microwave-assisted Au-ZnO NS, only 2.3 nm size of Au NPs were densely anchored on the oxide surface, and they provide suitable conditions for ionizing oxygen molecules and forming a thick EDL.

When the 2-CEES gas reacts with the ionized oxygen, the thickness of EDL is rapidly decreased because the electrons consumed for oxygen

ionization are regenerated and return to the conduction band of the metal oxides (Fig. 6d-e). For the oxidation reaction, the 2-CEES molecules are dissociated into two radical compounds according to Eq. (6). The thiyl radicals (R-S•) strongly interact with the gold surface, so they are readily adsorbed onto the anchored Au NPs. The oxidation of the adsorbed 2-CEES takes place via the Mars-van Krevelen mechanism, which is the reaction between the adsorbed species on the Au NP and the ionized oxygen at the perimeter sites of the Au NPs. Following these processes, the reaction kinetics can be expressed in equation (7) and (8). After oxidation, byproducts (CO_2, SO_2, and H_2O) are desorbed from the sensing materials.

$$ClCH_2CH_2SCH_2CH_3 \rightarrow ClCH_2CH_2\bullet + CH_3CH_2S\bullet \quad (6)$$

$$2ClCH_2CH_2\bullet + 8O^- \rightarrow 2CO_2 + Cl_2 + 4H_2O + 8e^- \quad (7)$$

$$2CH_3CH_2S\bullet + 13O^- \rightarrow 2SO_2 + 5H_2O + 2CO_2 + 13e^- \quad (8)$$

The change of the EDL affects the potential barrier (E_P) at a junction between the nanosheet particles (Fig. 6f-g). When the voltage is applied across the electrode, mobile charge carriers in one nanosheet are transported to another adjacent one following the electric field. However, if the junction E_P is too large to overcome, charge carriers cannot be migrated, increasing overall sensor resistivity. The bare porous ZnO NS has a thin EDL due to the low amounts of oxygen vacancy, so the E_P is relatively small, having a low baseline resistance. Even if the bare porous ZnO NS is reacted with 2-CEES molecules, the sensor resistance does not change much because there exists only a small amount of reaction sites. On the other hand, the Au-ZnO NS possesses a thick EDL by a lot of deficient oxygens, which produces a large E_P at the particle junction and high baseline resistance. When the sensor is exposed to the 2-CEES gas, 2-CEES molecules are efficiently reacted with enormous amounts of peripheral oxygen ions around Au NPs via Au-S interactions and the Mars-van-Krevelen reaction mechanism. It will significantly reduce the thickness of EDL and E_P, appearing as a dramatic decrease in resistance value. To sum up, the anchoring of Au NPs on oxides greatly enhances sensor responses by increasing the EDL thickness and junction potential barrier as well as fostering oxygen adsorption, dissociation, and ionization.

To validate the sensing capabilities in onsite environments, we have designed a portable type of sensor board integrating a developed sensor package (Fig. 7a). The dimension of the board is 34 mm × 22 mm with 4.82 g weight, which hardly affect the mobility of remote-controlled robotic systems, like a drone. The operating temperature of the sensor (400 °C) was regulated by an external power supply (2.0 V) connected to electrodes on a printed circuit board (PCB). The constant voltage (3.3 V) was also applied to the sensor circuit by another power source to measure the resistance level of the sensor. We measured the sensor resistance value by monitoring the divided potential to a constant resistance which was connected to the sensor circuit in serial. The sensor module was operated by communicating with a laptop by receiving commands through a serial program. The measured data was automatically saved in the built-in memory, which can be extracted to a laptop via a wired connection. Before gas exposure, the sensor module was assembled with a customized cover package to prevent mechanical damages from external stress. As shown in Fig. 7b, the target gas was prepared by the identical gas exposure system and flowed through the quartz tube. Through the system, gases with various concentrations were exposed to the sensor module (Fig. 7c). According to the extracted data, the sensor exhibited responses 62, 527, and 1087 for 2, 5, and 10 ppm of 2-CEES gases, respectively, which is comparable values measured by high-performance multimeter equipment. The sensor also rarely reacted to DMMP gases, which were 1.26 for 2 ppm, 1.96 for 5 ppm, and 2.72 for 10 ppm. In summary, we have confirmed outstanding sensitivity and selectivity toward the 2-CEES and verified the versatility of our sensor in the portable type of module through the measurement.

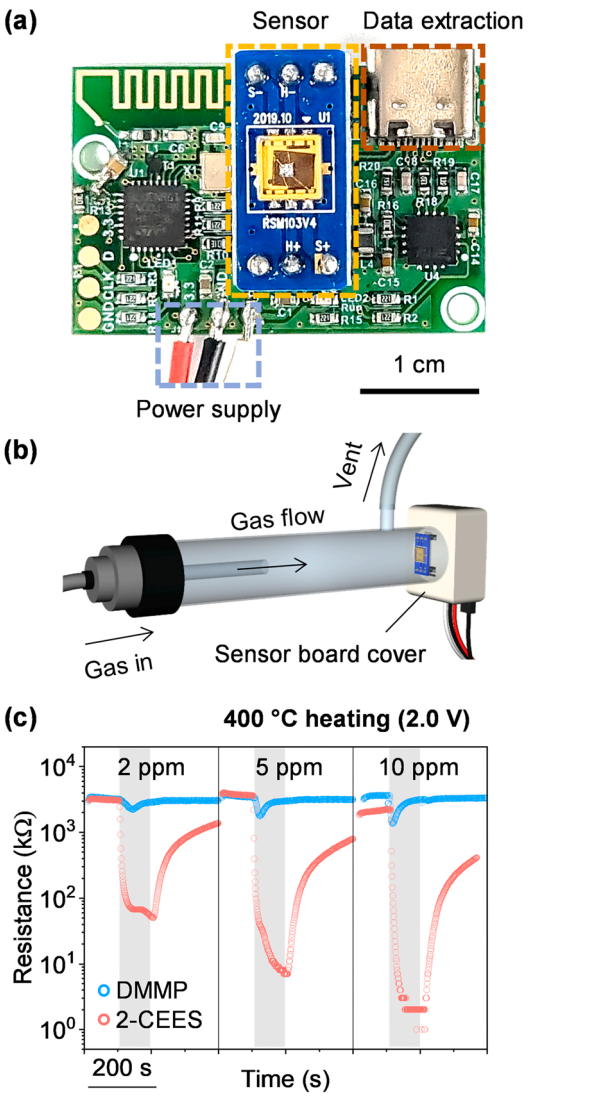

Fig. 7. Evaluation sensing performances of the Au-ZnO NS on a portable sensor board. (a) Picture of portable type of sensor module which has dimension of 34 mm × 22 mm and 4.82 g of weight. (b) Brief illustration of gas sensing experiment. The 2-CEES gas was supplied through a quartz tube. (c) The resistance curve of the Au-ZnO NS sensor under various concentration of 2-CEES and DMMP at 400 °C.

4. Conclusions

Herein, we report the microwave-assisted synthesis of a heterogeneous structure, i.e., Au nanoparticles anchored porous ZnO nanosheets, and its facile application as a CWA gas sensor with high sensitivity and selectivity toward 2-CEES vapor. When compared to conventional hydrothermal synthetic methods, a simple microwave irradiation approach provided a high-density decoration, narrow particle-size distribution, and strong structural anchoring of the Au nanoparticles on the surface of ZnO within a minute. The anchored Au nanoparticles affect the lattice structure of ZnO by inducing several defect sites and oxygen vacancies. Due to the high number of oxygen vacancies, a thicker electron depletion layer was formed, which contributed to the extremely large resistance change observed upon exposure to target molecules. The anchored Au nanoparticles also imparted the sulfur-selective detection properties, utilizing the high affinity between Au (111) and thiyl radicals. The effective adsorption of the decomposed 2-CEES products on Au nanoparticles promotes the Mars–van Krevelen reaction mechanism for complete oxidation. We expect that microwave-assisted anchoring of

noble metals on the metal oxide surfaces can offer great perspectives for the development of heteroatomic materials for a variety of electrochemical applications in sensing, energy, and catalysis.

CRediT authorship contribution statement

Minkyung Lee: Conceptualization, Investigation, Methodology, Writing – original draft, **Min Young Kim:** Conceptualization, Investigation, Methodology, Writing – original draft, Writing – review & editing **Jihee Kim:** Methodology, Investigation **Chul Oh Park:** Methodology, Investigation **Ha Eun Choa:** Methodology, Investigation **Seung Yong Lee:** Data curation, Investigation **Myung Kyu Park:** Data curation, Investigation **Hyegi Min:** Supervision, Conceptualization, Methodology, Investigation, Writing – original draft, Writing – review & editing **Kyu Hyoung Lee:** Methodology, Writing – review & editing, Supervision, Projectadministration, Methodology, Writing – review & editing. **Wooyoung Lee:** Supervision, Project administration, Methodology, Writing – review & editing.

Declaration of Competing Interest

The authors declare that they have no known competing financial interests or personal relationships that could have appeared to influence the work reported in this paper.

Data availability

Data will be made available on request.

Acknowledgments

This work is supported by the Agency for Defense Development (ADD, south Korea) (UG210063GD) and the Korea Initiative for fostering the University of Research and Innovation Program of the National Research Foundation (NRF, south Korea) (2020M3H1A1077207).

Appendix A. Supporting information

Supplementary data associated with this article can be found in the online version at doi:10.1016/j.snb.2023.133726.

References

[1] S. Chauhan, S. Chauhan, R. D'Cruz, S. Faruqi, K.K. Singh, S. Varma, M. Singh, V. Karthik, Chemical warfare agents, Environ. Toxicol. Pharmacol. 26 (2008) 113–122.
[2] Io Medicine, Chemical and Biological Terrorism: Research and Development to Improve Civilian Medical Response, The National Academies Press,, Washington, DC, 1999.
[3] C.W. Gardner, R. Wentworth, P.J. Treado, P. Batavia, G. Gilbert, Remote chemical biological and explosive agent detection using a robot-based Raman detector, Unmanned Syst. Technol. X 6962 (2008).
[4] A. Dey, Semiconductor metal oxide gas sensors: a review, Mater. Sci. Eng: B-Adv. Funct. Solid-State Mater. 229 (2018) 206–217.
[5] N. Barsan, D. Koziej, U. Weimar, Metal oxide-based gas sensor research: How to? Sens. Actuators B: Chem. 121 (2007) 18–35.
[6] R. Yoo, S. Cho, M.J. Song, W. Lee, Highly sensitive gas sensor based on Al-doped ZnO nanoparticles for detection of dimethyl methylphosphonate as a chemical warfare agent simulant, Sens. Actuators B: Chem. 221 (2015) 217–223.
[7] R. Yoo, S. Yoo, D. Lee, J. Kim, S. Cho, W. Lee, Highly selective detection of dimethyl methylphosphonate (DMMP) using CuO nanoparticles/ZnO flowers heterojunction, Sens. Actuators B: Chem. 240 (2017) 1099–1105.
[8] K.T. Alali, J.Y. Liu, K. Aljebawi, P.L. Liu, R.R. Chen, R.M. Li, H.Q. Zhang, L. M. Zhou, J. Wang, Electrospun n-p WO_3/CuO heterostructure nanofibers as an efficient sarin nerve agent sensing material at room temperature, J. Alloy Compd. 793 (2019) 31–41.
[9] Z. Yang, Y. Zhang, L. Zhao, T. Fei, S. Liu, T. Zhang, The synergistic effects of oxygen vacancy engineering and surface gold decoration on commercial SnO_2 for ppb-level DMMP sensing, J. Colloid Interfaces Sci. 608 (2022) 2703–2717.
[10] J. van den Broek, A.T. Guntner, S.E. Pratsinis, Highly selective and rapid breath isoprene sensing enabled by activated alumina filter, ACS Sens. 3 (2018) 677.
[11] I.C. Weber, H.P. Braun, F. Krumeich, A.T. Guntner, S.E. Pratsinis, Superior acetone selectivity in gas mixtures by catalyst-filtered chemoresistive sensors, Adv. Sci. 7 (2020).
[12] H. Jung, H. Min, J. Hwang, J. Kim, Y.S. Choe, H.S. Lee, W. Lee, Selective detection of sub-1-ppb level isoprene using Pd-coated In_2O_3 thin film integrated in portable gas chromatography, Appl. Surf. Sci. 586 (2022).
[13] H. Jung, W. Cho, R. Yoo, H.S. Lee, Y.S. Choe, J.Y. Jeon, W. Lee, Highly selective real-time detection of breath acetone by using ZnO quantum dots with a miniaturized gas chromatographic column, Sens. Actuators B: Chem. 274 (2018) 527–532.
[14] H. Hakkinen, The gold-sulfur interface at the nanoscale, Nat. Chem. 4 (2012) 443–455.
[15] T. Burgi, Properties of the gold-sulphur interface: from self-assembled monolayers to clusters, Nanoscale 7 (2015) 15553–15567.
[16] A. Cossaro, R. Mazzarello, R. Rousseau, L. Casalis, A. Verdini, A. Kohlmeyer, L. Floreano, S. Scandolo, A. Morgante, M.L. Klein, G. Scoles, X-ray diffraction and computation yield the structure of alkanethiols on gold(111), Science 321 (2008) 943–946.
[17] J.C. Love, L.A. Estroff, J.K. Kriebel, R.G. Nuzzo, G.M. Whitesides, Self-assembled monolayers of thiolates on metals as a form of nanotechnology, Chem. Rev. 105 (2005) 1103–1169.
[18] D.A. Giljohann, D.S. Seferos, W.L. Daniel, M.D. Massich, P.C. Patel, C.A. Mirkin, Gold nanoparticles for biology and medicine, Angew. Chem. Int. Ed. 49 (2010) 3280–3294.
[19] L.M. Demers, D.S. Ginger, S.J. Park, Z. Li, S.W. Chung, C.A. Mirkin, Direct patterning of modified oligonucleotides on metals and insulators by dip-pen nanolithography, Science 296 (2002) 1836–1838.
[20] W.S. Xu, H.M. Bao, H.W. Zhang, H. Fu, Q. Zhao, Y. Li, W.P. Cai, Ultrasensitive surface-enhanced Raman spectroscopy detection of gaseous sulfur-mustard simulant based on thin oxide-coated gold nanocone arrays, J. Hazard. Mater. 420 (2021).
[21] D.C. Onwudiwe, Microwave-assisted synthesis of PbS nanostructures, Heliyon 5 (2019).
[22] M.S. Choi, M.Y. Kim, A. Mirzaei, H.S. Kim, S.I. Kim, S.H. Baek, D.W. Chun, C. H. Jin, K.H. Lee, Selective, sensitive, and stable NO_2 gas sensor based on porous ZnO nanosheets, Appl. Surf. Sci. 568 (2021), 150910.
[23] Y.P. Liu, L.Y. Zhu, P. Feng, C.C. Dang, M. Li, H.L. Lu, L.M. Gao, Bimetallic AuPt alloy nanoparticles decorated on ZnO nanowires towards efficient and selective H_2S gas sensing, Sens. Actuators B: Chem. 367 (2022).
[24] S.S. Li, Y.K. Su, Improvement of the performance in Cr-doped ZnO memory devices via control of oxygen defects, RSC Adv. 9 (2019) 2941–2947.
[25] Y.Z. Chen, Z.H. Wang, H.F. Fu, D.M. Han, F.B. Gu, Insights into the effect of Au particle size on triethylamine sensing properties based on a Au-ZnO nanoflower sensor, J. Mater. Chem. C 10 (2022) 3318–3328.
[26] S.H. Hung, K. McKenna, First-principles investigation of the structure and properties of Au nanoparticles supported on ZnO, J. Phys. Chem. C 123 (2019) 21185–21194.
[27] Z.G. Xue, M.Y. Yan, X. Yu, Y.J. Tong, H. Zhou, Y.F. Zhao, Z.Y. Wang, Y.S. Zhang, C. Xiong, J. Yang, X. Hong, J. Luo, Y. Lin, W.X. Huang, Y.F. Li, Y.E. Wu, One-dimensional segregated single Au sites on step-rich ZnO ladder for ultrasensitive NO_2 sensors, Chem 6 (2020) 3364–3373.
[28] M. Mahanti, D. Basak, Enhanced ultraviolet photoresponse in Au/ZnO nanorods, Chem. Phys. Lett. 612 (2014) 101–105.
[29] S. Yang, L.J. Wang, Y.S. Yan, L.L. Yang, X. Li, Z.Y. Lu, H.J. Zhai, D.L. Han, P. W. Huo, Two hybrid Au-ZnO heterostructures with different hierarchical structures: towards highly efficient photocatalysts, Sci. Rep. 9 (2019).
[30] J.X. Liu, B.T. Qiao, Y.A. Song, Y.D. Huang, J.Y. Liu, Hetero-epitaxially anchoring Au nanoparticles onto ZnO nanowires for CO oxidation, Chem. Commun. 51 (2015) 15332–15335.
[31] Z.L. Wang, L.Z. Wang, Role of oxygen vacancy in metal oxide based photoelectrochemical water splitting, EcoMat 3 (2021).
[32] C. Gabriel, S. Gabriel, E.H. Grant, B.S.J. Halstead, D.M.P. Mingos, Dielectric parameters relevant to microwave dielectric heating, Chem. Soc. Rev. 27 (1998) 213–223.
[33] A.R. Puigdollers, P. Schlexer, S. Tosoni, G. Pacchioni, Increasing oxide reducibility: the role of metal/oxide interfaces in the formation of oxygen vacancies, ACS Catal. 7 (2017) 6493–6513.
[34] D.R. Baer, K. Artyushkova, H. Cohen, C.D. Easton, M. Engelhard, T.R. Gengenbach, G. Greczynski, P. Mack, D.J. Morgan, A. Roberts, XPS guide: charge neutralization and binding energy referencing for insulating samples, J. Vac. Sci. Technol. A 38 (2020).
[35] B. Bharti, S. Kumar, H.N. Lee, R. Kumar, Formation of oxygen vacancies and Ti^{3+} state in TiO_2 thin film and enhanced optical properties by air plasma treatment, Sci. Rep. 6 (2016).
[36] R. Biswas, B. Banerjee, M. Saha, I. Ahmed, S. Mete, R.A. Patil, Y.R. Ma, K.K. Haldar, Green approach for the fabrication of Au/ZnO nanoflowers: a catalytic aspect, J. Phys. Chem. C 125 (2021) 6619–6631.
[37] N. Abdullayeva, C.T. Altaf, M. Mintas, A. Ozer, M. Sankir, H. Kurt, N.D. Sankir, Investigation of strain effects on photoelectrochemical performance of flexible ZnO electrodes, Sci. Rep. 9 (2019).
[38] N. Gogurla, A.K. Sinha, S. Santra, S. Manna, S.K. Ray, Multifunctional Au-ZnO plasmonic nanostructures for enhanced UV photodetector and room temperature NO sensing devices, Sci. Rep. 4 (2014).
[39] C. Drouilly, J.M. Krafft, F. Averseng, S. Casale, D. Bazer-Bachi, C. Chizallet, V. Lecocq, H. Vezin, H. Lauron-Pernot, G. Costentin, ZnO oxygen vacancies

formation and filling followed by in situ photoluminescence and in situ EPR, J. Phys. Chem. C 116 (2012) 21297–21307.
[40] L.M. Lin, J.Y. Liu, J. Lv, S.J. Shen, X.P. Wu, D.C. Wu, Y. Qu, W.F. Zheng, F.C. Lai, Correlation between native defects and morphological, structural and optical properties of ZnO nanostructures, J. Alloy Compd. 695 (2017) 1523–1527.
[41] W. Niu, H. Zhu, X.F. Wang, J.D. Ye, F.Q. Song, J.F. Zhou, S.L. Gu, Y. Shi, Y.B. Xu, R. Zhang, Identification of defect-related emissions in ZnO hybrid materials, Appl. Phys. Lett. 107 (2015).
[42] N.S. Ferreira, J.M. Sasaki, R.S. Silva, J.M. Attah-Baah, M.A. Macedo, Visible-light-responsive photocatalytic activity significantly enhanced by active $[V_{Zn}+V_O^{\cdot}]$ defects in self-assembled ZnO nanoparticles, Inorg. Chem. 60 (2021) 4475–4496.
[43] M. Tang, J.X. Shang, Y. Zhang, Oxygen vacancy and doping atom effect on electronic structure and optical properties of Cd_2SnO_4, RSC Adv. 8 (2018) 640–646.
[44] J.P. Wang, Z.Y. Wang, B.B. Huang, Y.D. Ma, Y.Y. Liu, X.Y. Qin, X.Y. Zhang, Y. Dai, Oxygen vacancy induced band-gap narrowing and enhanced visible light photocatalytic activity of ZnO, ACS Appl. Mater. Inter. 4 (2012) 4024–4030.
[45] M. Al-Hashem, S. Akbar, P. Morris, Role of oxygen vacancies in nanostructured metal-oxide gas sensors: a review, Sens. Actuators B: Chem. 301 (2019).
[46] J.Y. Zhou, J.L. Bai, H. Zhao, Z.Y. Yang, X.Y. Gu, B.Y. Huang, C.H. Zhao, L. M. Cairang, G.Z. Sun, Z.X. Zhang, X.J. Pan, E.Q. Xie, Gas sensing enhancing mechanism via doping-induced oxygen vacancies for gas sensors based on indium tin oxide nanotubes, Sens. Actuators B: Chem. 265 (2018) 273–284.
[47] J. Lee, Y. Choi, B.J. Park, J.W. Han, H.S. Lee, J.H. Park, W. Lee, Precise control of surface oxygen vacancies in ZnO nanoparticles for extremely high acetone sensing response, J. Adv. Ceram. 11 (2022) 769–783.
[48] J.H. Lee, H. Jung, R. Yoo, Y. Park, H.S. Lee, Y.S. Choe, W. Lee, Real-time selective detection of 2-chloroethyl ethyl sulfide (2-CEES) using an Al-doped ZnO quantum dot sensor coupled with a packed column for gas chromatography, Sens. Actuators B: Chem. 284 (2019) 444–450.
[49] Z.J. Li, H. Li, Z.L. Wu, M.K. Wang, J.T. Luo, H.D. Torun, P.A. Hu, C. Yang, M. Grundmann, X.T. Liu, Y.Q. Fu, Advances in designs and mechanisms of semiconducting metal oxide nanostructures for high-precision gas sensors operated at room temperature, Mater. Horiz. 6 (2019) 470–506.
[50] P. Esser, W. Gopel, Physical adsorption on single-crystal zinc-oxide, Surf. Sci. 97 (1980) 309–318.
[51] M.Z. Ahmad, A.Z. Sadek, K. Latham, J. Kita, R. Moos, W. Wlodarski, Chemically synthesized one-dimensional zinc oxide nanorods for ethanol sensing, Sens. Actuators B: Chem. 187 (2013) 295–300.
[52] W.S. Zhang, Y.N. Wang, Z.R. Xu, High sensitivity and non-background SERS detection of endogenous hydrogen sulfide in living cells using core-shell nanoparticles, Anal. Chim. Acta 1094 (2020) 106–112.
[53] G. Yang, J. Nanda, B.Y. Wang, G. Chen, D.T. Hallinan, Self-assembly of large gold nanoparticles for surface-enhanced Raman spectroscopy, ACS Appl. Mater. Interfaces 9 (2017) 13457–13470.
[54] H. Liu, A.M. Schwenke, F. Kretschmer, S. Hoeppener, U.S. Schubert, Gold nanoparticle cluster arrays for high-performance SERS substrates fabricated by electro-oxidative lithography, ChemNanoMat 2 (2016) 781–785.
[55] M.A. Saqlain, A. Hussain, M. Siddiq, A.A. Leitao, A. DFT, plus U study of the Mars Van Krevelen mechanism of CO oxidation on Au/TiO_2 catalysts, Appl. Catal. A: Gen. 519 (2016) 27–33.
[56] S. Scire, L.F. Liotta, Supported gold catalysts for the total oxidation of volatile organic compounds, Appl. Catal. B: Environ. 125 (2012) 222–246.
[57] X.Q. Cao, J. Zhou, H.N. Wang, S. Li, W. Wang, G.W. Qin, Abnormal thermal stability of sub-10 nm Au nanoparticles and their high catalytic activity, J. Mater. Chem. A 7 (2019) 10980–10987.
[58] J.H. Shim, B.J. Lee, Y.W. Cho, Thermal stability of unsupported gold nanoparticle: a molecular dynamics study, Surf. Sci. 512 (2002) 262–268.
[59] D.E. Wurster, E. Oh, J.C.T. Wang, Determination of the mechanism for the decrease in zinc-oxide surface-area upon high-temperature drying, J. Pharm. Sci. 84 (1995) 1301–1307.
[60] Y. Fan, K. Li, X.G. Ren, W.L. Yan, C.J. Zhu, Y.F. Zhao, W. Zeng, Z.L. Chen, S. L. Wang, A highly selective gas sensor based on the WO_3/WS_2 van der Waals heterojunction for the 2-chloroethyl ethyl sulfide (2-CEES) sensing application, J. Mater. Chem. C 9 (2021) 17496–17503.
[61] R. Yoo, D. Lee, S. Cho, W. Lee, Doping effect on the sensing properties of ZnO nanoparticles for detection of 2-chloroethyl ethylsulfide as a mustard simulant, Sens. Actuators B: Chem. 254 (2018) 1242–1248.
[62] H.M. Aliha, A.A. Khodadadi, Y. Mortazavi, The sensing behaviour of metal oxides (ZnO, CuO and Sm_2O_3) doped-SnO_2 for detection of low concentrations of chlorinated volatile organic compounds, Sens. Actuators B: Chem. 181 (2013) 637–643.
[63] L.A. Patil, V.V. Deo, M.D. Shinde, A.R. Bari, D.M. Patil, M.P. Kaushik, Improved 2-CEES sensing performance of spray pyrolized Ru-$CdSnO_3$ nanostructured thin films, Sens. Actuators B: Chem. 191 (2014) 130–136.
[64] L.A. Patil, V.V. Deo, M.D. Shinde, A.R. Bari, M.P. Kaushik, Sensing of 2-chloroethyl ethyl sulfide (2-CEES) – a CWA simulant – using pure and platinum doped nanostructured $CdSnO_3$ thin films prepared from ultrasonic spray pyrolysis technique, Sens. Actuators B: Chem. 160 (2011) 234–243.
[65] S.Y. Jeong, Y.K. Moon, J.K. Kim, S.W. Park, Y.K. Jo, Y.C. Kang, J.H. Lee, A general solution to mitigate water poisoning of oxide chemiresistors: bilayer sensors with Tb_4O_7 overlayer, Adv. Funct. Mater. 31 (2021), 2007895.
[66] X.J. Zhu, X.T. Chang, S.K. Tang, X.Q. Chen, W.X. Gao, S.C. Niu, J.F. Li, Y.C. Jiang, S.B. Sun, Humidity-tolerant chemiresistive gas sensors based on hydrophobic CeO_2/SnO_2 heterostructure films, ACS Appl. Mater. Interfaces 14 (2022) 25680–25692.
[67] J. Hong, S. Lee, J. Seo, S. Pyo, J. Kim, T. Lee, A highly sensitive hydrogen sensor with gas selectivity using a PMMA membrane-coated Pd nanoparticle/single-layer graphene hybrid, ACS Appl. Mater. Interfaces 7 (2015) 3554–3561.
[68] M.S. Yao, W.X. Tang, G.E. Wang, B. Nath, G. Xu, MOF thin film-coated metal oxide nanowire array: significantly improved chemiresistor sensor performance, Adv. Mater. 28 (2016) 5229.
[69] I.N. Martyanov, K.J. Klabunde, Photocatalytic oxidation of gaseous 2-chloroethyl ethyl sulfide over TiO_2, Environ. Sci. Technol. 37 (2003) 3448–3453.
[70] X.X. Chen, Y.B. Shen, X.X. Zhong, T.T. Li, S.K. Zhao, P.F. Zhou, C. Han, D.Z. Wei, Y. S. Shen, Synthesis of ZnO nanowires/Au nanoparticles hybrid by a facile one-pot method and their enhanced NO_2 sensing properties, J. Alloy Compd. 783 (2019) 503–512.
[71] O. Lupan, V. Postica, N. Wolff, J. Su, F. Labat, I. Ciofini, H. Cavers, R. Adelung, O. Polonskyi, F. Faupel, L. Kienle, B. Viana, T. Pauporte, Low-temperature solution synthesis of Au-modified ZnO nanowires for highly efficient hydrogen nanosensors, ACS Appl. Mater. Interfaces 11 (2019) 32115–32126.
[72] U.T. Nakate, R.N. Bulakhe, C.D. Lokhande, S.N. Kale, Au sensitized ZnO nanorods for enhanced liquefied petroleum gas sensing properties, Appl. Surf. Sci. 371 (2016) 224–230.
[73] H.T. Wang, Y.Y. Li, C.C. Wang, Y. Li, J.H. Bai, Y.Y. Liu, L.S. Zhou, F.M. Liu, K. Shimanoe, G.Y. Lu, N-pentanol sensor based on ZnO nanorods functionalized with Au catalysts, Sens. Actuators B: Chem. 339 (2021).

Minkyung Lee received a Master's degree in materials science and engineering at Yonsei university in 2012. Since 2012, she is a senior researcher of Chem-bio Technology Center Team1 in Agency for Defense Development (ADD) in Korea. She is currently a Ph.D. candidate at the department of materials science and engineering in Yonsei University under the supervision of Prof. Wooyoung Lee. She is currently studying on nanostructured metal oxide semiconductor gas sensors.

Min Young Kim is a Ph.D. candidate in the Department of Materials Science and Engineering at Yonsei University in Seoul, South Korea. She received her M.S. degree in the Department of Energy Science at Sungkyunkwan University in Suwon, South Korea, in 2018. Her research interests are high-performance thermoelectric materials and functional oxides.

Jihee Kim received a Bachelor's degree in Materials Science and Engineering from Pusan National University in 2021. She is a M.S candidate at the Department of Materials Science and Engineering in Yonsei University under the supervision of Prof. Wooyoung Lee. She is currently studying metal-oxide-semiconductor gas sensors.

Chul Oh Park is currently an integrated graduate student in the Materials Science and Engineering at Yonsei University in Seoul, Korea. He received his bachelor in Materials Science and Engineering from Yonsei University in 2020. His field of interests are thermoelectric and gas sensors based on oxide semiconductor.

Ha Eun Choa is currently an integrated graduate student in the Materials Science and Engineering at Yonsei University in Seoul, Korea. She received her bachelor in Chemical and Biomolecular Engineering from Sogang University in 2022. Her field of interests are gas sensors and catalysts based on metal oxide semiconductors, and thermoelectrics.

Seung Yong Lee got a Ph.D. degree in the Department of Energy Science at Sungkyunkwan university in 2021. He has been currently working in Korea Initiative for fostering University of Research and Innovation program in Yonsei University in Seoul since 2021. His research interests are metal-oxide materials.

Myung Kyu Park graduated with a BS in chemical engineering from Yonsei University in Seoul Korea in 1985 and received a Ph.D. in same university with a research of gas purification by plasma decomposition in 2003. Now, he is working for the department of Chem-Bio Technical Center in Agency for Defense Development (ADD) in Daejon as a principal researcher with the research of Chemical and Biological Detection.

Hyegi Min earned a Ph.D. degree in Chemical Engineering at Ulsan National Institute of Science and Technology (UNIST) in 2021. He is currently a research professor in the Korea Initiative for fostering University of Research & Innovation (KIURI) institute of the Department of Materials Science and Engineering at Yonsei University. His research has focused on the low dimensional carbon nanomaterials, nanopore detection of individual ions/molecules, heterogeneous catalysis, metal-oxide-semiconductor gas sensors, and nanoelectronics.

Kyu Hyoung Lee is currently a professor in the Department of Materials Science and Engineering at Yonsei University in Seoul, Korea. He received his Ph.D. in ceramic engineering from Yonsei University in 2005. From 2005–2007, he worked as a postdoctoral research fellow at Nagoya University. Since 2007, he has been a research staff member and since 2010 project leader at the Samsung Advanced Institute of Technology. His research activity has focused on the development of high-performance thermoelectric materials and functional oxides.

Wooyoung Lee is a professor of the Department of Materials Science and Engineering and the Director of Center for Super Critical Material Industrial Technology (MOTIE) at Yonsei University in Korea. He received a BS degree in Metallurgical Engineering in 1986, a MS

degree in Metallurgical Engineering from the Yonsei University in 1988. He received a Ph. D. degree in Physics from University of Cambridge, United Kingdom in 2000. He is a regular member of National Academy of Engineering of Korea. He was a member of National Science & Technology Council and a director in Korea Israel Industrial R&D Foundation. In recent years, his research interests have centered on hydrogen sensors, various metal oxide semiconducting gas sensors, and breath analyzers. He is also studying thermoelectric materials and devices, and permanent magnets. He has received a number of awards in nano-related research areas and a Service Merit Medal (2008) from the Government of Korea due to contribution on the development of intellectual properties. He has authored and co-authored over 200 publications, and has edited three special books on nano-structured materials and devices.